

Article

An Investigation of the Damage Mechanism of Multilayer Liquid-Containing Protective Structure under Combined Blast Wave and Fragment Loading

Zeqing Fan ^{1,2}, Xiaobin Li ^{1,2}, Tao Huang ³ and Wei Chen ^{1,2,*} 

¹ Key Laboratory of High Performance Ship Technology, Wuhan University of Technology, Ministry of Education, Wuhan 430063, China

² School of Naval Architecture, Ocean and Energy Power Engineering, Wuhan University of Technology, Wuhan 430063, China

³ The 710 Research Institute, China Shipbuilding Industry Corporation, Yichang 443003, China

* Correspondence: whutcw01@126.com

Abstract: A multilayer liquid-containing protective structure is composed of a liquid tank, ceramic, a honeycomb sandwich and homogeneous steel. This structure has superior resistance to combined blast wave and fragment loading. Due to the relatively complicated construction of the structure, the inner damage, energy absorption and the protection characteristics of the multilayer liquid-containing protective structure need to be further studied. In this paper, a multilayer liquid-containing structural model is constructed, the dynamic response process of multilayer liquid-containing structure under combined blast wave and fragment loading is analyzed, and the damage and energy absorption characteristics of each layer structure are investigated. In addition, the effects of the charge mass and fragment form on the structural failure modes and energy absorption characteristics are discussed. The results indicate that different modes of damage occur in each layer structure. The front plate of the liquid tank sustains the most damage and absorbs the most energy, and the honeycomb sandwich absorbs the second most energy. The damage area of the front plate and the degree of compression collapse of the honeycomb sandwich increase with increasing charge mass. When the charge mass is small, the damage mode of the multilayer liquid-containing structure is greatly affected by fragments, and the damage effect of the blast wave increases with increasing charge mass. For a constant charge mass, the degree of damage to the protective structure is minimally impacted by the fragment weight, and the degree of damage can be substantially reduced by reducing the number of fragments.

Keywords: multilayer liquid-containing structure; protection mechanism; honeycomb sandwich; combined loading



Citation: Fan, Z.; Li, X.; Huang, T.; Chen, W. An Investigation of the Damage Mechanism of Multilayer Liquid-Containing Protective Structure under Combined Blast Wave and Fragment Loading. *J. Mar. Sci. Eng.* **2023**, *11*, 2327. <https://doi.org/10.3390/jmse11122327>

Academic Editor: Spyros Hirdaris

Received: 10 November 2023

Revised: 29 November 2023

Accepted: 7 December 2023

Published: 8 December 2023



Copyright: © 2023 by the authors. Licensee MDPI, Basel, Switzerland. This article is an open access article distributed under the terms and conditions of the Creative Commons Attribution (CC BY) license (<https://creativecommons.org/licenses/by/4.0/>).

1. Introduction

Anti-ship weaponry can penetrate a side of a vessel and explode inside a cabin, resulting in damage to the cabin structure, casualties and equipment. In severe cases, this weaponry may cause the entire vessel to sink and lose combat effectiveness, posing a serious threat to the vitality of the vessel [1–3]. It is critical to improve the passive protection capabilities of vessels, and installing armor on the bulkheads is a highly efficient approach. Important compartments, such as command rooms, fuel tanks and ammunition tanks, are especially susceptible to attacks due to their critical nature. Considering multiple factors, including construction costs, lightweight design and environmental sustainability, the targeted design of protective structures for important cabins is a crucial approach for enhancing the overall vitality of vessels.

In addition to traditional steel, liquid tanks, ceramic materials, lightweight sandwich structures and negative Poisson's ratio metamaterials are widely used in protective armor design [4,5]. Ceramic materials are leveraged to reinforce composite armor due to their

impact resistance and exceptional hardness and strength [6,7]. Serjouei et al. [8] found that increasing backplane stiffness can improve the protective performance of ceramic composite armor through experiments. Lightweight sandwich structures with low manufacturing costs, high specific strength and high specific stiffness are frequently used in the design of protective structures [9–12]. Zhou et al. [13] experimentally studied the impact resistance of a Nomex honeycomb sandwich structure subjected to the strong dynamic loading of projectiles and revealed the deformation process and breaking mode of the sandwich plate. Patel [14] studied the blast performance of a square honeycomb sandwich panel via simulation and explored the effect of honeycomb height on performance. The simulation results showed that increasing the core height improves blast resistance by reducing back face deflection. Liquid tanks are effective for protection against fragments and blast waves, and they have been the focus of protective structure research [15,16]. Ren et al. [17] experimentally and numerically studied the penetration of a projectile in a water-filled container with aluminum target plates. Four types of typical failure modes for the plates in the water-filled container were identified through the results. Combining different structures to form multilayer protective structures is a popular research topic in vessel protection design. Xu et al. [18] designed a type of liquid-filled honeycomb structure reinforced via a Kevlar fiber tube and determined the mechanism by which the structure resists fragmentation.

The internal explosion of an anti-ship weapon can generate various damage elements, such as blast waves, high-speed fragments and quasistatic pressures. The combined damage is more serious than the sum of damage caused by the blast and fragment loading separately [19,20]. Zhang et al. [21] investigated the dynamic response of I-core sandwich panels under combined blast wave and fragment loading via simulation methods. The results demonstrated that the damage caused by combined blast loading is more severe than that caused by bare blast loading. Cai et al. [22] carried out an experimental investigation into the failure mechanisms of sandwich panels with multilayered aluminum foam/UHMWPE laminate cores under combined blast and fragment loading. The results showed that the sandwich panels suffer much more destructive damage under combined loading than under bare blast loading. Li et al. [23] examined the performance of aluminum honeycomb core sandwich panels against combined loading. The results revealed that combined loading aggravates the damage of the sandwich panel and that the performance is sensitive to the parameters of the sandwich geometries. Jin et al. [24] evaluated the damage of a liquid cabin structure under combined blast wave and fragment loading created by charge explosion with preset fragments. The results showed that the free surface can decrease the intensity of the pressure pulse and reduce the deformation of the liquid cabin, and a large numerical fragment causes a stronger shock wave and more severe structural damage than a dense fragment cluster. Huang et al. [25] combined the advantages of various structures to design a multilayer liquid-containing protective structure, and experiments have proven that the protective structure is effective for resisting combined blast wave and fragment loading. However, the extent of internal structure damage, the function of each layer structure and the pattern of the transmission of blast waves and fragments in the protective structure require further study.

To illustrate the inner damage, energy absorption and protection mechanism of the multilayer liquid-containing protective structure, in this study, a multilayer liquid-containing structure model is constructed, its response process under combined blast wave and fragment loading is investigated and the effects of charge mass and fragment form on its protective performance are explored. The main structure of this paper is as follows: In Section 2, a numerical simulation model of a multilayer liquid-containing protective structure against combined blast wave and fragment loading is established using the S-ALE method. The material models utilized are listed in detail, and the accuracy of the simulation method is verified using experiments. In Section 3, the action of fragments and blast waves and the damage mode of each layer of the structure are given, and the protection mechanism of the structure is analyzed. The key factors affecting the protection performance of

the protective structure are analyzed, and the effects of charge mass and fragment weight and number on the deformation mode, failure mode and protection performance of the protective structure are discussed. In Section 4, the investigation of the protective structure under combined blast wave and fragment loading is summarized, and some conclusions are drawn.

2. Protective Structure Model and Method

2.1. Protective Structure Model

A conceptual figure of the experiment performed by Huang [25] is shown in Figure 1a. In this experiment, the multilayer liquid-containing protective structure was used as the protective bulkhead of a cabin and compared with an ordinary steel bulkhead. The size of the protective bulkhead was $2.15\text{ m} \times 3\text{ m}$, and the warhead exploded at a distance of 0.5 m from the center of the protective bulkhead. The warhead was a shelled warhead with a length of 450 mm , a diameter of 130 mm and a charge of a 6.12 kg TNT explosive. The test results showed that the multilayer liquid-containing protective structure provided adequate protection, as the rear plate deformed marginally.

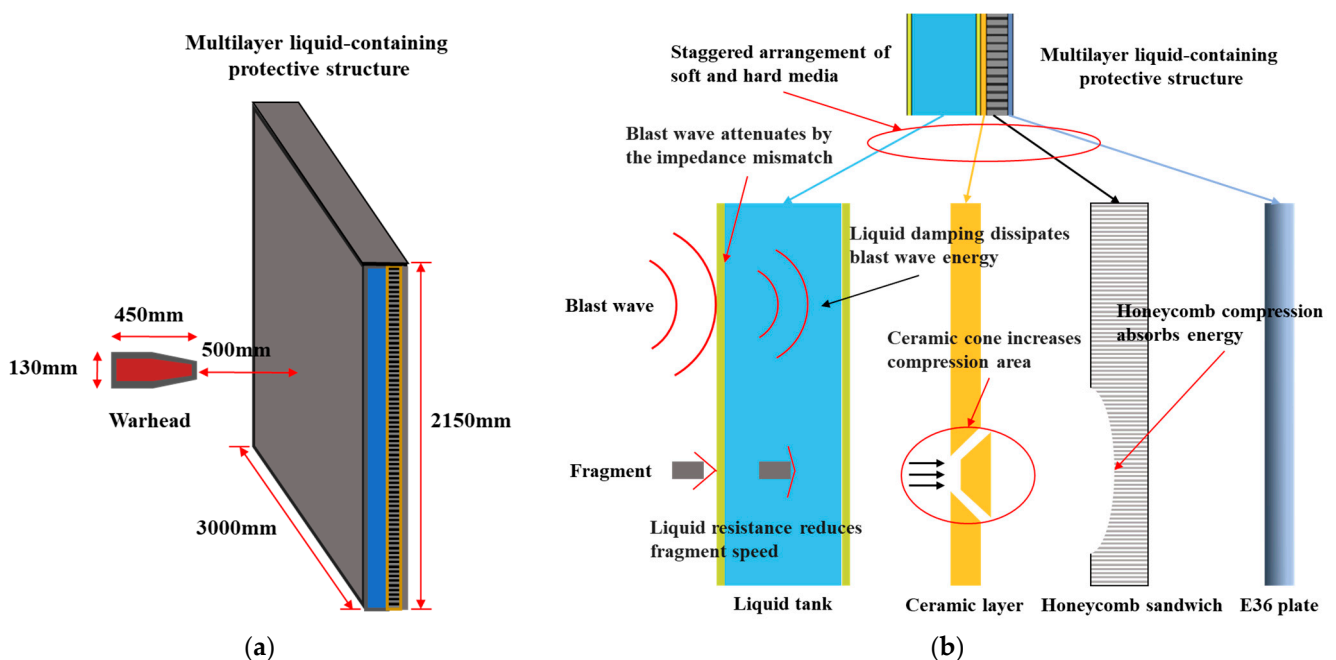


Figure 1. (a) A conceptual figure of the experiment performed by Huang [25]. (b) Theoretical analysis of the protection mechanism.

The protection mechanism of a multilayer liquid-containing protective structure under combined loading needs to be further studied, and a preliminary analysis of it is conducted at the theoretical level, as shown in Figure 1b. At the interface of distinct media, the stress wave will be transmitted and reflected, and the intensity of the transmission reflection wave depends on the degree of the impedance mismatch [26]. The protective structure consists of a staggered distribution of soft and hard media, and the stress wave will be attenuated by this distribution. A liquid tank can convert the concentrated load into a distributed load, dissipate blast wave energy via liquid damping and reduce fragment velocity via liquid resistance. The impact of the ceramic layer produces a ceramic cone, reducing the kinetic energy of the fragments [27], and the ceramic cone can increase the compressed area of the honeycomb layer. The specific energy absorption of the honeycomb sandwich layer is large [28], the compression of the honeycomb sandwich can absorb a lot of energy and the backplane sustains minimal damage. Thus, a simulation method is utilized to further study the protection mechanism. The scale of the test model is m level, and the scale of the

honeycomb layer and ceramic layer inside the protective structure is mm level, which is a significant scale disparity. If the finite element model is established directly according to the size of the test model, the number of girds will reach tens of millions, making calculation challenging. Therefore, a small-size finite element model is used to study the protection mechanism of the protective structure. To ensure the reliability of the results, a number of experiments are used to verify the accuracy of the simulation method.

To study the protection mechanism of a multilayer liquid-containing protective structure under combined blast wave and fragment loading, the protective structure model and warhead model shown in Figure 2 are established. The protective structure model comprises four distinct layers. The initial layer is the liquid tank, which measures 60 mm in width, and its front and back plates are made of a 6061-T6 aluminum alloy with a thickness of 4 mm. The subsequent layer is a SiC ceramic with a thickness of 5 mm. The third layer is a honeycomb sandwich layer with a width of 20 mm. Within this layer, the honeycomb aluminum sandwich consists of regular hexagonal cells, each with a side length of 5 mm and a cell thickness of 0.1 mm. The outermost layer is a marine E36 steel plate with a thickness of 5 mm. The charge is a cylindrical TNT explosive, with an equivalent of 200 g, a diameter of 50 mm and a length of 61 mm. To simulate combined blast wave and fragment loading, 69 prefabricated fragments measuring 6 mm × 6 mm × 3 mm are positioned at the upper end of the cylindrical explosive. The vertical distance from the explosive to the lower surface of the protective structure is 100 mm. Due to the symmetry of the problem, a 1/4 model is selected as the calculation model, and the size of the protective structure is 200 mm × 200 mm. The air domain is set outside the protective structure. The mesh in the region where the combined loading directly impacts the protective structure is locally refined, while the progressive mesh is utilized to mesh the air and water. For the mesh convergence analysis of a structure with a honeycomb sandwich, the mesh size is generally 1–5 mm [14,18]. The encrypted region is assigned a mesh size of 1 mm, while the remaining regions are assigned a mesh size of 2–4 mm. With approximately 600,000 structural meshes and 2.5 million fluid meshes, the total number of meshes in the finite element model is approximately 3.1 million, and LS-DYNA is used to perform simulations.

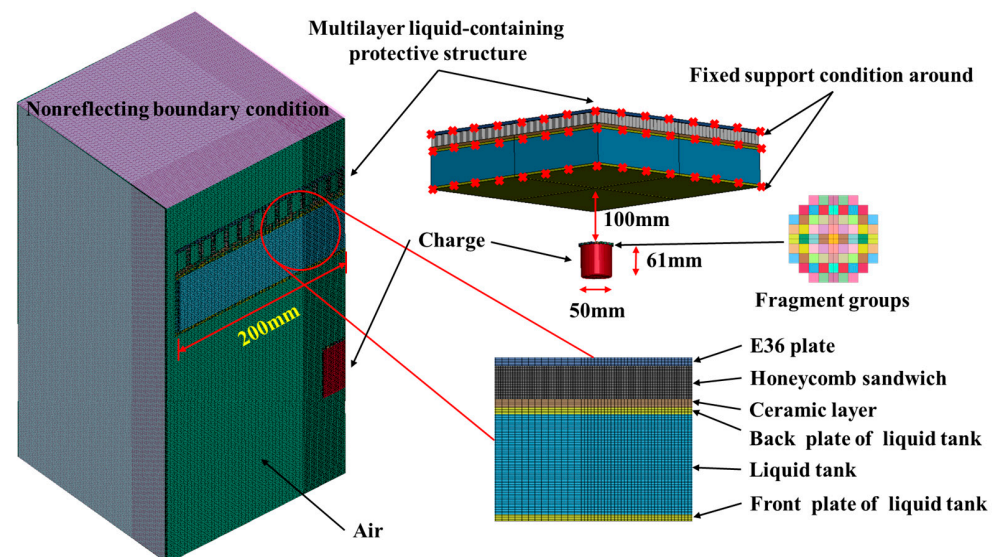


Figure 2. Numerical simulation model [25] (Different colored squares are fragment groups).

The protective structure is surrounded by fixed support boundary conditions, while the outer surface of the air domain is subjected to non-reflective boundary conditions to simulate an infinite air domain. To define the coupling between structure and liquid, the keyword *LAGRANGE IN SOLID is applied. The contact mode between the fragments and the protective structure is defined as erosion contact. The bonding be-

tween the ceramic layer and the liquid tank backplane is simulated by the keyword *CONTACT_SURFACE_TO_SURFACE_TIEBREA. The contact mode is defined by the keyword *CONTACT_TIED_SHELL_EDGE_TO_SURFACE to simulate the bonding between a honeycomb core cell and its adjacent cells. Because deformation and stacking may occur between the cells of the honeycomb core during fragment penetration, the keyword *CONTACT_AUTOMATIC_SINGLE_SURFACE is used to simulate the self-contact between the honeycomb core cells.

2.2. Material Model and Parameters

The outermost plate is made of E36 steel, and the front and back plates of the liquid tank and the honeycomb sandwich are made of a 6061-T6 aluminum alloy. The material parameters of E36 steel and 6061-T6 aluminum alloy are shown in Table 1. The two materials are described by the Cowper–Symonds constitutive model. The relationship between the yield stress, plastic strain and strain rate is as follows:

$$\sigma_d = \left(\sigma_0 + \beta \frac{E E_{tan}}{E - E_{tan}} \epsilon_p \right) \left[1 + \left(\frac{\dot{\epsilon}}{C} \right)^{\frac{1}{P}} \right] \tag{1}$$

where σ_d is the dynamic yield stress, σ_0 is the initial yield strength, $\dot{\epsilon}$ is the strain rate, ϵ_p is the effective plastic strain, E is the tangent modulus, E_{tan} is the tangent modulus, C and P are the strain rate parameters and β is the hardening parameter.

Table 1. Material parameters of E36 steel [29] and 6061-T6 aluminum alloy [30].

| Material | ρ /(kg/m ³) | E /GPa | ν | σ_0 /MPa | β | C /s ⁻¹ | P |
|----------|------------------------------|----------|-------|-----------------|---------|----------------------|------|
| E36 | 7850 | 209 | 0.295 | 430 | 1 | 5698.7 | 1.92 |
| 6061-T6 | 2704 | 70 | 0.33 | 276 | 1 | 5101 | 1 |

The fragment material is 40Cr steel, which is analyzed using the Johnson–Cook constitutive model. The material parameters of 40Cr steel are shown in Table 2. The yield stress can be expressed as follows:

$$\sigma_y = \left[A + B(\epsilon_p)^n \right] \left[1 + c \ln \left(\frac{\dot{\epsilon}_p}{\dot{\epsilon}_0} \right) \right] \left[1 - \left(\frac{T - T_r}{T_m - T_r} \right)^m \right] \tag{2}$$

where σ_y is the dynamic flow stress, A is the static yield limit, B is the strain hardening modulus, c is the strain rate coefficient, n is the strain hardening index of the elastomer, m is the thermal softening index, ϵ_p is the equivalent plastic strain, $\dot{\epsilon}_p$ the equivalent plastic strain rate, $\dot{\epsilon}_0$ is the reference strain rate, T is the absolute temperature of the material, T_m is the melting temperature and T_r is the room temperature.

Table 2. Material parameters of 40Cr steel [31].

| ρ /(kg/m ³) | E /GPa | A /MPa | B /MPa | n | c | m | T_m /K | T_r /K | $\dot{\epsilon}_0$ /s ⁻¹ | ϵ_p |
|------------------------------|----------|----------|----------|------|------|-----|----------|----------|-------------------------------------|--------------|
| 7850 | 205 | 894 | 764 | 0.35 | 0.06 | 1.5 | 1802 | 298 | 0.001 | 0.28 |

The ceramic layer is made of SiC ceramic. The ceramic material strength model is described using the JH2 constitutive equation, which is widely used to simulate the properties of brittle materials, such as ceramics. The material parameters of SiC ceramic are shown in Table 3.

Table 3. Material parameters of the SiC ceramic [32].

| Parameter | Data | Parameter | Data | Parameter | Data | Parameter | Data |
|---------------------------------|--------|-----------------------------|---------|-----------|------|--------------------|------|
| $\rho / (\text{kg}/\text{m}^3)$ | 3163 | $T_{\text{HEL}}/\text{GPa}$ | 13.0 | A | 0.96 | $EPSI$ | 1.0 |
| G/GPa | 183 | K_1/GPa | 204.785 | B | 0.35 | $BETA$ | 1.0 |
| T/GPa | 0.37 | K_2/GPa | 0 | C | 0 | D_1 | 0.48 |
| HEL/GPa | 14.567 | K_3/GPa | 0 | M | 1.0 | D_2 | 0.48 |
| $P_{\text{HEL}}/\text{GPa}$ | 5.9 | S_{fmax} | 0.8 | N | 0.65 | μ_{HEL} | 0 |

The TNT explosive utilizes the JWL state equation. The material parameters of TNT are shown in Table 4. The specific form of the JWL state equation is as follows:

$$p_T = A(1 - \frac{\omega}{r_1 v})e^{-R_1 v} + B(1 - \frac{\omega}{r_2 v})e^{-R_2 v} + \frac{\omega e}{v} \tag{3}$$

where A, B, R_1, R_2 and ω are constants. p_T, v and e are the pressure, relative volume and specific internal energy, respectively.

Table 4. Material parameters of TNT [33].

| $\rho / (\text{kg}/\text{m}^3)$ | $D_{\text{CJ}} / (\text{m}/\text{s})$ | $P_{\text{CJ}} / \text{GPa}$ | E_0 / GPa | A / GPa | B / GPa | R_1 | R_2 | ω |
|---------------------------------|---------------------------------------|------------------------------|--------------------|------------------|------------------|-------|-------|----------|
| 1630 | 6930 | 21 | 6.0 | 373.77 | 3.73 | 4.15 | 0.9 | 0.35 |

The linear polynomial state equation is applied to air, while the Gruneisen state equation is applied to water. The material parameters of air and water are shown in Table 5.

Table 5. Material parameters of air [34] and water [35].

| Air | Data | Air | Data | Water | Data | Water | Data |
|---------------------------------|------|-----------------|-------------------|---------------------------------|--------|-----------------|---------------------|
| $\rho / (\text{kg}/\text{m}^3)$ | 1.18 | C_4 | 0.4 | $\rho / (\text{kg}/\text{m}^3)$ | 998.21 | γ_0 | 0.35 |
| C_0/Pa | 0 | C_5 | 0.4 | $C / (\text{m}/\text{s})$ | 1647 | A | 0 |
| C_1/Pa | 0 | C_6 | 0 | S_1 | 1.921 | E_0/Pa | 2.895×10^5 |
| C_2/Pa | 0 | E_0/Pa | 2.5×10^5 | S_2 | -0.096 | V_0 | 1.0 |
| C_3/Pa | 0 | V_0 | 1.0 | S_3 | 0 | | |

2.3. Numerical Method Verification

To validate the accuracy of the numerical method employed in this paper, a number of experiments are reproduced using the numerical method. The experiment performed by Zhang [36] concerns the deformation and failure modes of fixed support square plates under combined blast wave and fragment loading. A comparison of the ultimate response of the Q235 steel plate between the experiment and simulation is depicted in Figure 3. The plate is flexed overall, and a significant break forms in the center of the plate. In the vicinity of the break, there are continuous bullet holes, scattered bullet holes and bulging bullet marks. The simulation results indicate that the diameter of the break in the center is 43 mm, which is 7% larger than the test value of 40 mm. The center of the break exhibits the maximum deflection of the fixed square plate. As illustrated in Figure 3c, the maximum deflection of the simulation is 27.3 mm, which is 9.2% larger than the test value of 25 mm. The problems in the test, such as the explosive position not completely facing the center of the plate, the asymmetric arrangement of prefabricated fragments and the boundary of the target plate that cannot be completely fixed due to the loosening of bolts, must be considered. The numerical simulation method presented in this paper effectively simulates the behavior of a fixed steel plate under combined blast wave and fragment loading.

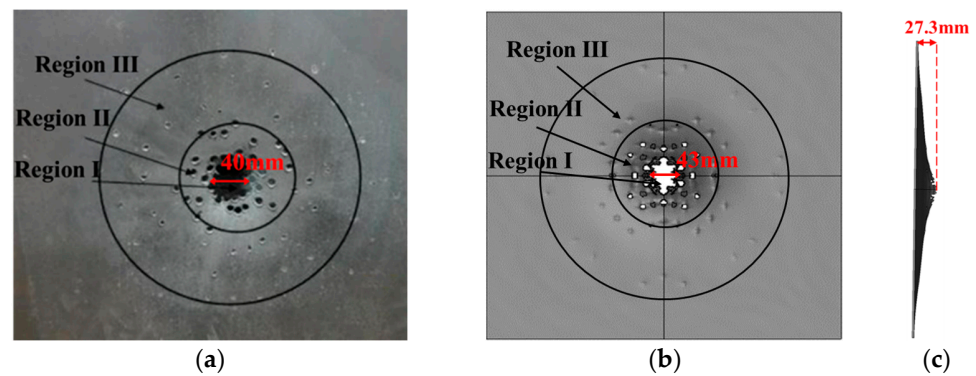


Figure 3. Comparison of the experimental and numerical results of the steel plate under combined loading. (a) Experimental results [36]. (b) Simulation results. (c) Numerical maximum deflection of the steel plate.

Li [37] experimentally investigated the structural response of the liquid tank under the action of a cylindrical bare charge. The experimental condition is numerically simulated utilizing the numerical method in this paper. Figure 4a depicts a comparison between the results obtained from the simulation and the experiment. The experiment and numerical simulation indicate that the front plate of the liquid tank experiences overall small deflection deformation. The deformation area and curve are consistent, and the central maximum deflection error is 9.7%. Consequently, the numerical simulation method employed in this study can be deemed reliable. Zhong [38] experimentally investigated the response of a cylindrical projectile penetrating a ceramic/tank composite structure, and four conditions were reproduced using the numerical method in this paper. Figure 4b illustrates a comparison between the results of the simulation and the test. According to the results of the simulation and experiment, the head of the projectile was severely eroded, and the projectile had assumed a mushroom shape with coarse deformation. The calculated values of the residual velocity and residual length of the projectile were compared with the experimental values. The residual velocity and residual length deviation rates of the projectile were both below 12%. Based on the above comparison, the reliability of the numerical simulation method utilized in this paper can be proven.

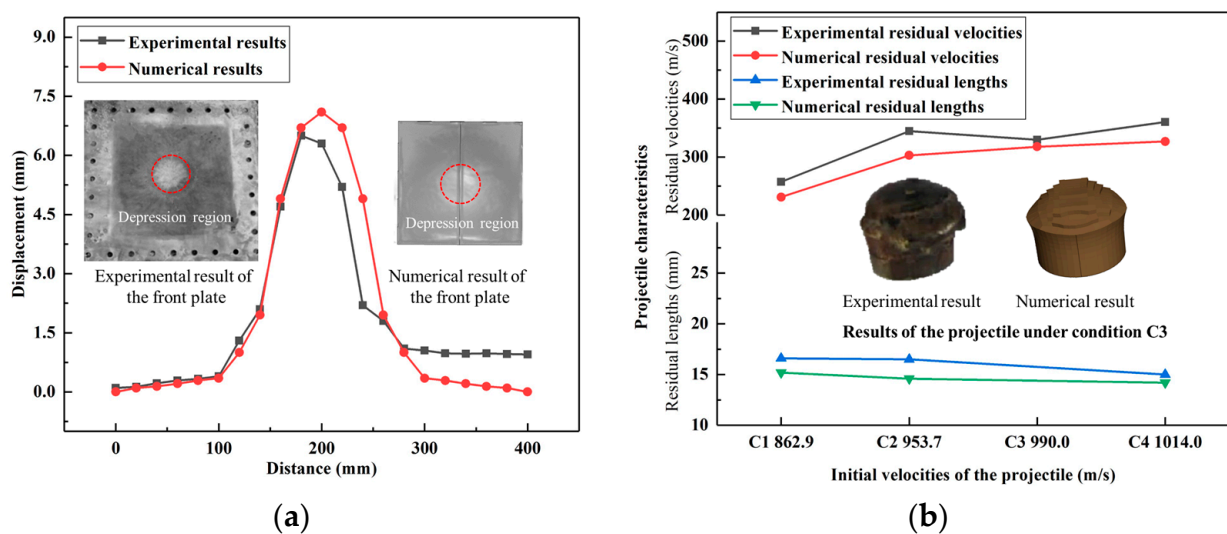


Figure 4. (a) Comparison of the experimental and numerical results of the front plate [37]. (b) Comparison of the experimental and numerical results of the projectile [38].

3. Results and Discussion

3.1. Structural Damage

The interaction process of the multilayer liquid-containing protective structure under combined blast wave and fragment loading is delineated into two stages. One stage involves fragments that are propelled by the blast wave generated by the detonation of the TNT explosive. In the other stage, the protective structure interacts with the combined loading. Figure 5 depicts the fragment dispersion process induced by the blast wave. At 10 μs , the fragments initiate a velocity that increases for the blast wave generated by the explosion. At 30 μs , the fragments exhibit fan shapes as they move forward. This phenomenon can be attributed to the blast wave propagating forward as a spherical wave, which accelerates the fragments in the central region before accelerating those in the edge region. At 60 μs , the central fragments maintain a relatively stable motion attitude due to the alignment of the velocity direction with the propagation direction of the explosion wave. In contrast, the fragments in the edge region undergo lateral flipping. At 90 μs , the overall divergence angle of the fragments and the distance between the central and perimeter fragments continue to increase with the increasing disparity in the speed and attitude of the fragments.

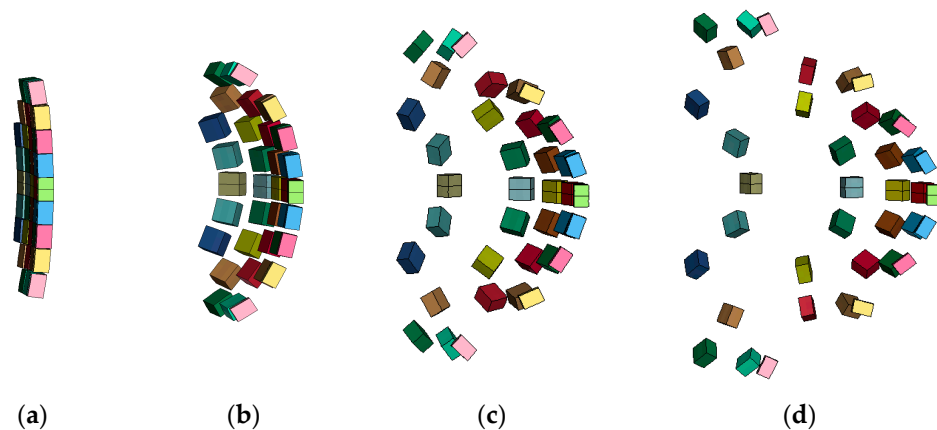


Figure 5. Projectile process of fragments (Different colored squares are fragment groups). (a) 10 μs ; (b) 30 μs ; (c) 60 μs ; (d) 90 μs .

The response of the multilayer liquid-containing protective structure under combined blast wave and fragment loading is illustrated in Figure 6. At 100 μs , the fragments in the central region initially reach the front plate of the liquid tank. A significant break takes place in the center of the front plate due to penetration. At 150 μs , the fragments from the central area enter the liquid tank and start to move in the liquid. Fragments from the edge region generate scattered holes around the large break in the front plate. Concurrently, secondary fragments, formed by the fragments penetrating the front plate, enter the liquid tank. At 300 μs , the central fragments traverse the liquid to reach the back plate of the liquid tank, while the slowest fragments in the edge reach the front plate. The effect of these fragments on the front plate is the formation of bulging bullet marks due to their low kinetic energy. Concurrently, as a result of cavitation caused by the entry of numerous fragments into the liquid tank, liquid extrudes from the front plate of the tank, resulting in apparent membrane bulging damage. Additionally, the back plate of the tank experiences local deflection deformation as a consequence of the central fragments and water extrusion. The significant deformation of the back plate causes the ceramic layer to retract, which compresses the honeycomb layer. The ceramic layer breaks and cracks in the local area. The honeycomb layer as a whole undergoes bending and deformation, while the central region is crushed.

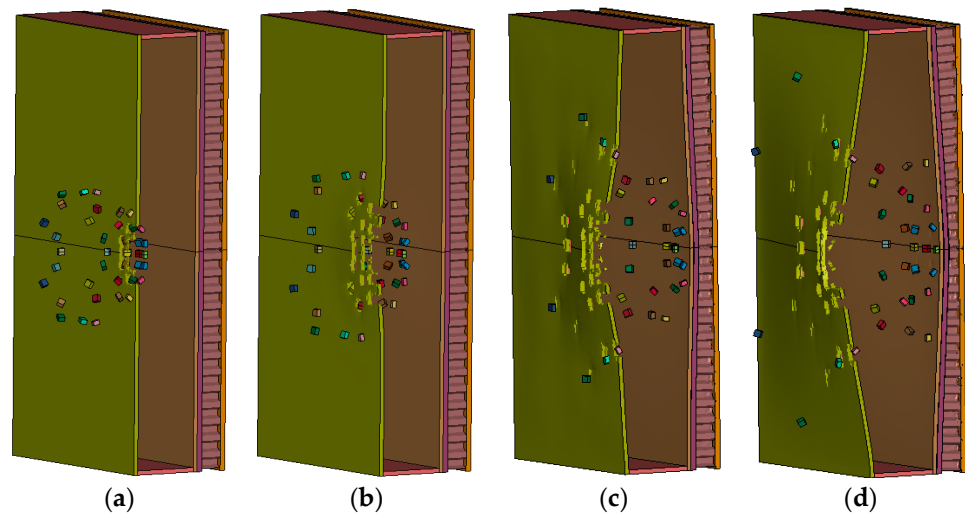


Figure 6. Response process of multilayer liquid-containing protective structure under combined loading (Different colored squares are fragment groups). (a) 100 μs ; (b) 150 μs ; (c) 300 μs ; (d) 600 μs .

Variations in fluid pressure throughout the process are categorized into two components: air pressure variation and water pressure variation. The evolution of the air pressure is illustrated in Figure 7. At 10 μs , the cylindrical TNT swiftly converts into byproducts of high-temperature and high-pressure detonations. The air is perpetually compressed by the detonation product, which generates an explosion wave. The pressure is greatest at the center of the detonation at this moment. At 30 μs , the pressure at the epicenter of the explosion decreases progressively as the detonation wave propagates. The pressure at the front end of the blast wave is considerably greater than that at the rear end because the blast wave interacts with the fragments and is compressed. The propagation velocity of the blast wave at the front end is considerably slower than that at the rear end because the fragments are propelled. The general shape of the blast wave is a semiellipsoid at this time. At 60 μs , the fragments are propelled forward by the blast wave, and a portion of the blast wave surpasses the fragments. The general shape of the blast wave is apple-like. The propagation speed of the blast wave is considerably greater than that of the fragments during the early stages of the explosion. At 80 μs , the blast wave reaches the front plate of the liquid tank, generating interactions.

The fluctuations in water pressure in the liquid tank are illustrated in Figure 8. At 90 μs , the fragments at the center impact the front plate of the liquid tank, resulting in the dispersion of water pressure within the liquid tank in the form of a spherical wave at the center of the impact point. At 110 μs , as an increasing number of fragments enter the tank, the pressure waves generated by their collision with the water undergo superposition, causing the diameter of the spherical wave within the liquid tank to gradually increase. Simultaneously, the blast wave that bypasses the fragments impacts the front plate, causing the front plate to deflect inward and compress the water to form a pressure wave. At 130 μs , the spherical wave is transmitted to the back plate and subsequently reflected. The velocity attenuation of the central fragments is more pronounced when subjected to the pressure wave that is reflected. The surrounding fragments surpass the velocity of the central fragments. The reflected pressure wave reaches the front plate at 160 μs , causing the front plate to deform outward and reflect again. The pressure wave oscillates repeatedly in the liquid tank, dissipating a large amount of explosion energy in the water through damping.

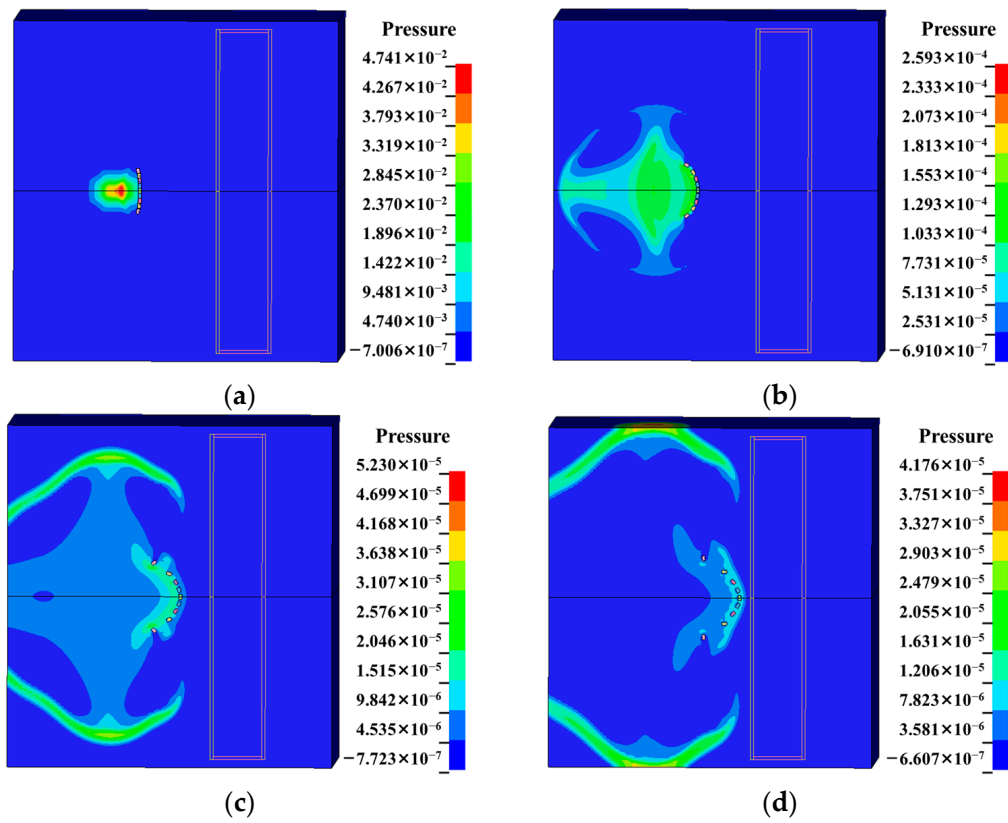


Figure 7. Evolution in air pressure (unit: 100 GPa). (a) 10 μ s; (b) 30 μ s; (c) 60 μ s; and (d) 80 μ s.

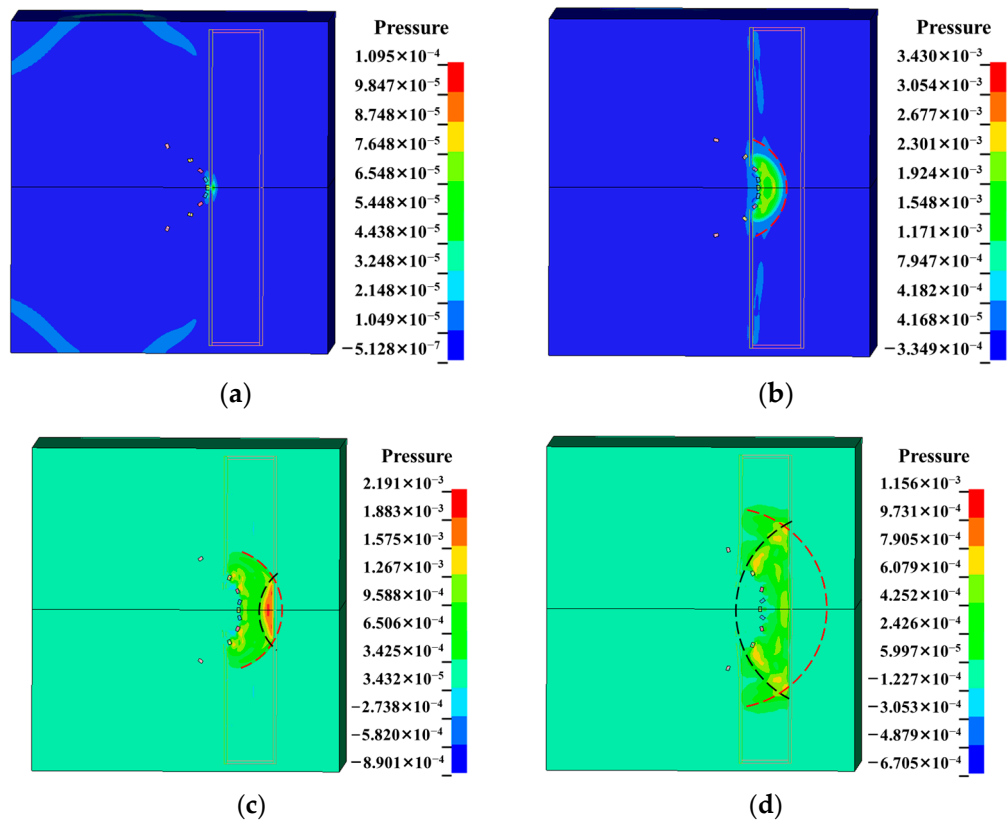


Figure 8. Evolution of water pressure (unit: 100 GPa). (a) 90 μ s; (b) 110 μ s; (c) 130 μ s; and (d) 160 μ s.

3.2. Effect of Charge Mass

The charge mass is an important factor affecting the protective properties and damage mode of the multilayer liquid-containing protective structure under combined blast wave and fragment loading. This factor significantly alters the velocity of the fragments and directly influences the intensity of the blast wave. To investigate the impact of varying charge masses on the protective ability of the protective structure, numerical simulations are conducted under the following five conditions: 100 g, 200 g, 300 g, 400 g, and 500 g. All other parameters remain constant.

The velocity measuring points are distributed on the four fragments along the explosive center to the periphery. Figure 9a illustrates the peak velocities attained by the velocity measuring points for various charge masses. The velocity of the fragment at the center is the fastest, while that at the edge is merely 60–70% of that at the center. The disparity in velocity between the edge fragment and the center fragment increases with increasing charge mass. The explanation for this phenomenon is that the blast wave is more concentrated at the center than at the edge, and the peak overpressure is greater. The overturning attitude of the edge fragments varies greatly during motion, and the acting surface of the blast wave decreases when the diffraction is serious. Pressure measuring points are distributed throughout the fluid body along the path of the propagation center of the blast wave. The peak pressure curves for each measuring point at various charge masses are depicted in Figure 9b. The diagram illustrates that the pressure peak values of the measuring points in air and water increase with increasing charge mass. The peak pressures of the measuring points in air increase at relatively slow rates, while the blast wave pressure in water varies noticeably. The reason for this phenomenon is that the blast wave in air transfers a substantial amount of energy to the fragments. Because the combined blast wave and fragment loading generate the blast wave pressure in water, the pressure in water is more sensitive to the various charge masses.

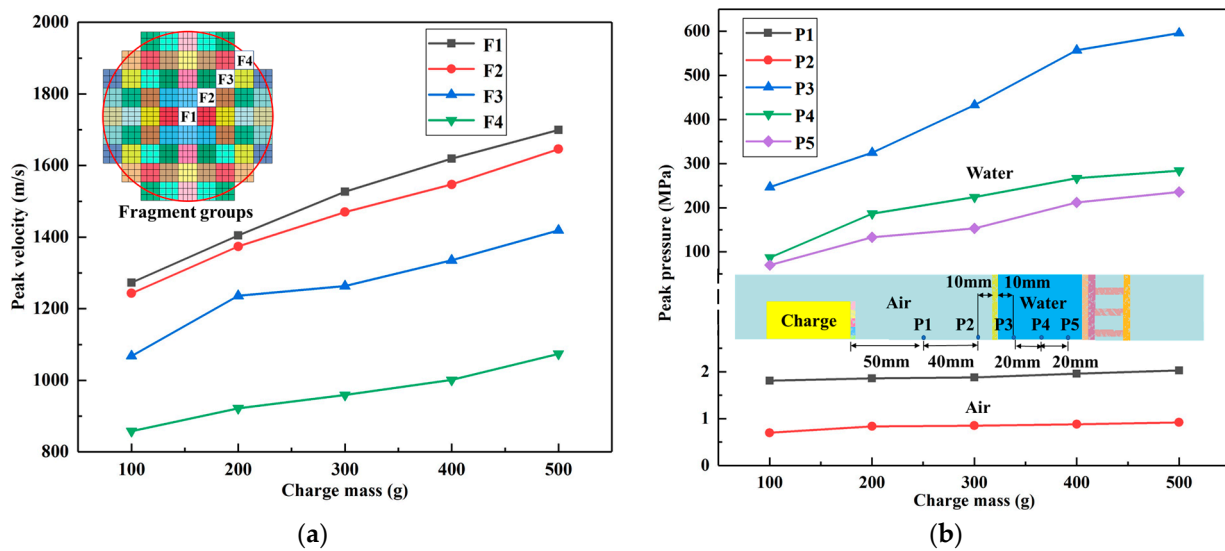


Figure 9. Data of measuring points under different charge masses. (a) Peak velocities of fragments at different positions (Different colored squares are fragment groups). (b) Peak pressure of different measuring points.

The ultimate responses of the protective structure at various charge masses are illustrated in Figure 10. The damage modes of the front plate of the liquid tank are as follows: a large break, continuous bullet holes, dispersed bullet holes and bulging bullet marks that extend from the center to the edge. Concurrently, outward deflection deformation is produced. The magnitude of the break and the deflection increase as the charge mass increases. The damage mode of the back plate of the liquid tank is minor inward deflection

deformation. Concurrently, distended bullet marks emerge in the center. Deflection deformation and the depth of the bullet marks increase with increasing charge mass. The ceramic layer moves backward as a whole with the back plate and compresses the honeycomb layer. The predominant damage mechanism observed in the honeycomb layer is local collapse erosion in the central region, accompanied by an overall increase in bending deformation as the charge mass increases.

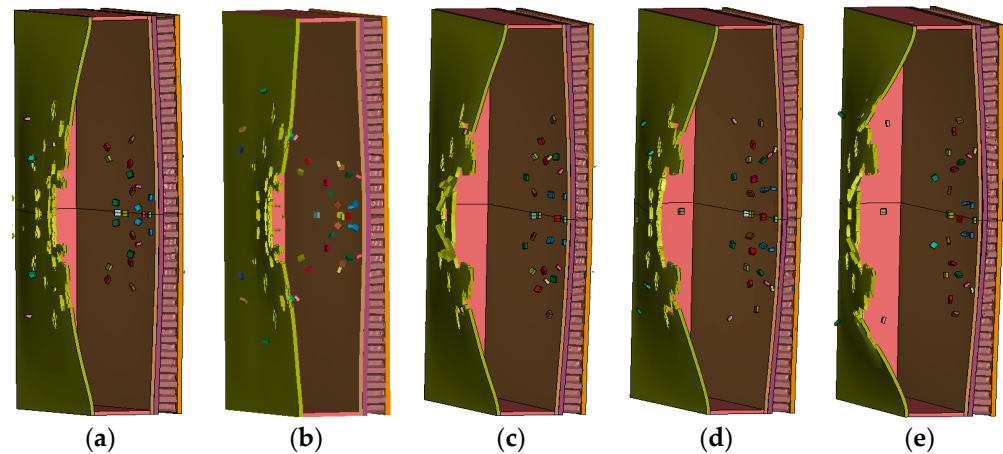


Figure 10. Ultimate response of the protective structure under different charge masses. (a) 100 g; (b) 200 g; (c) 300 g; (d) 400 g; (e) 500 g.

The ultimate deflection deformation modes of the front plate and E36 steel plate at various charge masses are illustrated in Figure 11a. The forward direction of fragments is taken as the positive direction. The final deflection deformation direction of the front plate is opposite to the positive direction. This phenomenon is the result of the front plate deforming outwardly through expansion due to the fragments in the water causing cavitation and due to the extrusion of the blast wave. When the charge mass is low, the damage mode of the front plate is more affected by fragments. This damage mode is mainly represented by fragment perforation in the center and overall outward deflection deformation. The deflection deformation of the front plate increases as the charge mass ranges from 100 g to 400 g, while the increasing range diminishes gradually. The front plate deflection remains relatively constant at charge mass of 400 g and 500 g, as the impact of the explosion wave counterbalances the influence of fragmentation. The deflection deformation of the E36 steel plate is aligned with the positive direction, and deflection deformation increases with increasing charge mass.

The energies of the blast wave and fragments are converted into the plastic deformation energy of the structure. However, some of the energy is damped and dissipated in the liquid tank. The deformation energy absorption and its corresponding proportion for each layer of the protective structure are illustrated in Figure 11b, considering various charge masses. The figure illustrates that the front plate of the liquid tank exhibits the highest energy absorption, with a total energy absorption ratio exceeding 70%. The honeycomb sandwich contributes 15% to the energy absorption. As the charge mass increases, there is a progressive decrease in the energy absorption ratio of the front plate, accompanied by a gradual increase in the energy absorption ratio of the back plate and honeycomb layer. The damage and deformation of the front plate become relatively stable at a charge mass of 400 g. This finding suggests that the energy absorption has essentially reached a state of saturation. When fragment penetration is absent, the energy absorption effect of the ceramic layer is constrained, as the energy absorption ratio remains essentially stable. In conjunction with Figure 11a, the maximum central deflection for the outermost E36 steel plate does not surpass 4 mm, and the absorption of deformation energy is negligible.

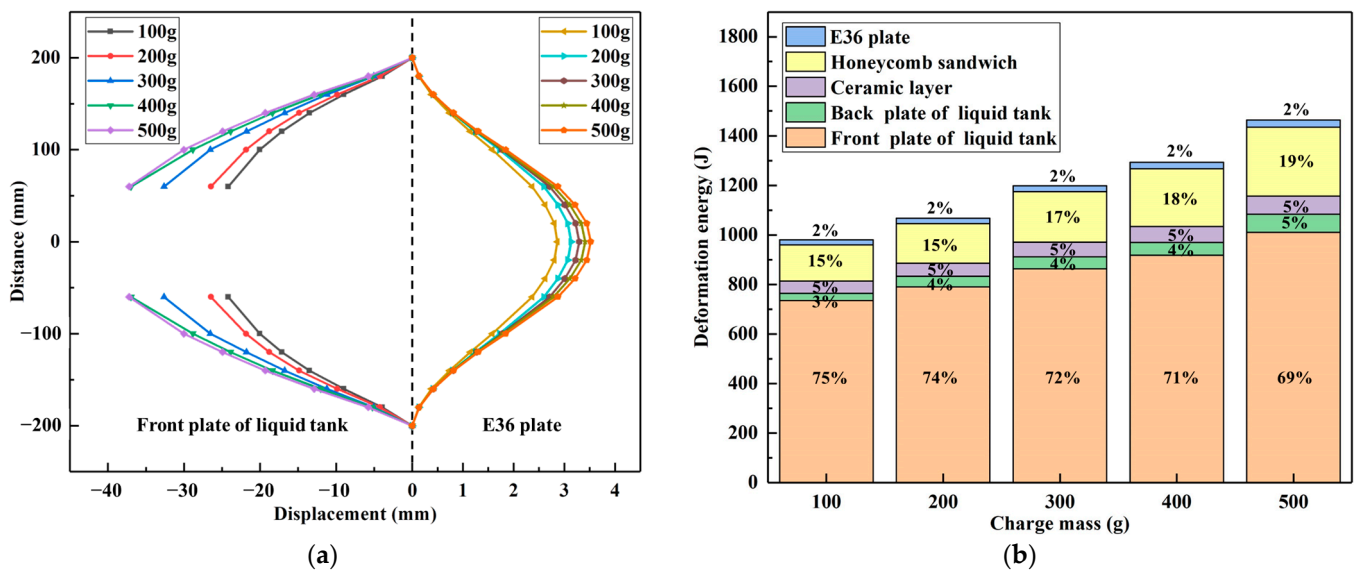


Figure 11. Structural response results under different charge masses. (a) Final deformation of foremost and rearmost plates. (b) Energy of deformation absorption and its proportion for each layer structure.

3.3. Effect of Fragment Form

Under combined loadings, the fragment group is an important factor affecting the damage to the protective structure. The influence of the parameter variations on the damage mode of the protective structure cannot be disregarded. The weight of a single fragment and the distribution range of the whole fragment group obviously affect the deformation and failure modes of the protective structure. The calculation conditions shown in Table 6 are further developed to explore the influences of the quality and quantity of fragments on the damage results of the protective structure.

Table 6. Numerical cases for different fragment weights and numbers.

| Case No. | Fragment Size/mm | Weight of a Single Fragment/g | Number of Fragments |
|----------|------------------|-------------------------------|---------------------|
| C1 | 6 × 6 × 2 | 0.565 | 69 |
| C2 | 6 × 6 × 3 | 0.848 | 69 |
| C3 | 6 × 6 × 4 | 1.130 | 69 |
| C4 | 6 × 6 × 6 | 1.696 | 69 |
| C5 | 6 × 6 × 3 | 0.848 | 49 |
| C6 | 6 × 6 × 3 | 0.848 | 25 |
| C7 | 6 × 6 × 3 | 0.848 | 9 |

3.3.1. Effect of Fragment Weight

The time history curves of the fragment velocities for various fragment weights are depicted in Figure 12. The velocities of fragments are significantly impacted by variations in fragment weight when the charge mass remains constant. Under the four conditions of C1, C2, C3 and C4, the kinetic energies of the central fragments are 825.1 J, 819.2 J, 743.3 J and 621.4 J, respectively; the edge fragments have the following kinetic energies: 389.3 J, 340.4 J, 217.8 J and 162.2 J, respectively. Under the condition of a constant charge mass, the velocity and kinetic energy of the fragment decrease with increasing fragment weight. The velocity reduction rate values and kinetic energy reduction rate of the border fragments are greater than those of the center fragments.

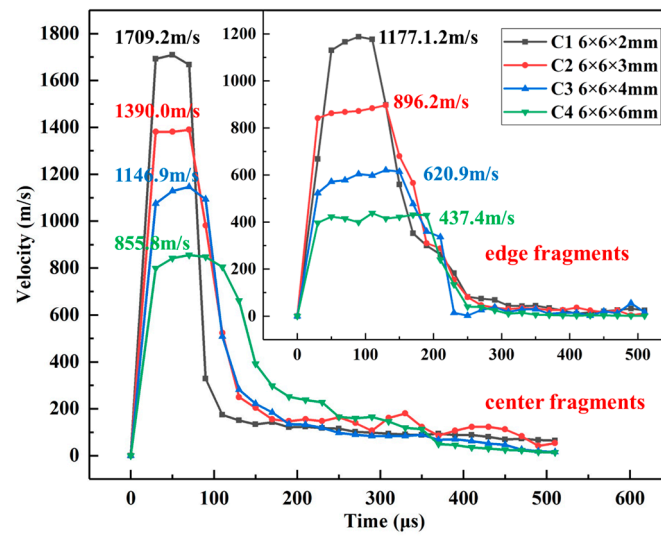


Figure 12. Fragment velocity time history curve of different fragment weights.

The ultimate response of the multilayer liquid-containing protective structure and the damage results of the front plate under different fragment weights are depicted in Figure 13. From the response results of deformation and failure, it can be observed that the damage modes of each layer of the structure under the four conditions are essentially the same. The front plate of the liquid tank experiences large outward deformation as a whole, and there are cavities and local fragment perforations in the central area. The back plate of the tank experiences inward plastic deformation as a whole, and fragment impact marks appear in the central area. The ceramic layer undergoes deformation in conjunction with the back plate, resulting in the compression of the honeycomb layer. The honeycomb layer exhibits bending deformation throughout, with honeycomb collapse failure occurring in the central region. The E36 steel plate remains undamaged, exhibiting minimal plastic deformation.

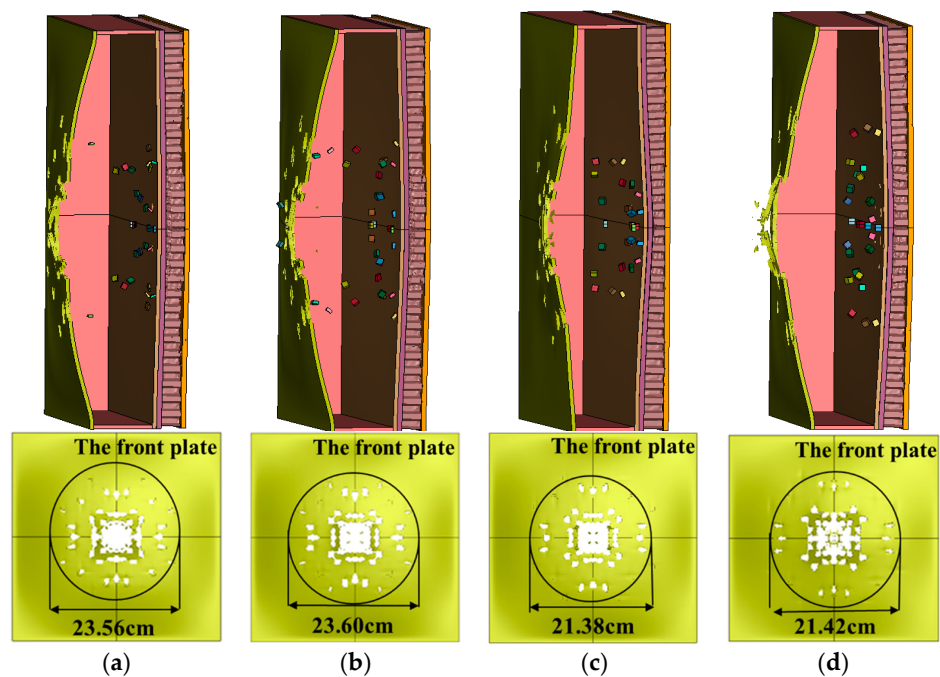


Figure 13. Ultimate response of multilayer liquid-containing protective structure and damage results of the front plate under different fragment weights: (a) C1— $6 \times 6 \times 2$ mm; (b) C2— $6 \times 6 \times 3$ mm; (c) C3— $6 \times 6 \times 4$ mm; and (d) C4— $6 \times 6 \times 6$ mm.

The ultimate deformation characteristics of the front plate and E36 steel plate under varying fragment weights are illustrated in Figure 14a. The front plate experiences a maximum deflection ranging from 22 mm to 30 mm under the conditions of C1, C2, C3 and C4. The plastic deformation of the front plate diminishes marginally as the fragment weight decreases. The maximum deflection at the center of condition M4 is marginally greater than that observed under condition C3. The reason is that the break caused by large weight fragments at the center of the front plate is bulky, while more water is extruded on the front plate. Due to the reduced velocity and kinetic energy of the large fragment, the front plate deflects less under C4 conditions than under C3 conditions. The E36 steel plate experiences negligible deformation under all conditions, with a maximum deflection of 4 mm. Figure 14b illustrates the absorption of deformation energy and its corresponding proportion for each layer within the protective structure. The primary energy-absorbing structure is the front plate of the liquid tank, followed by the honeycomb structure. The combined energy absorption of these two components constitutes 90% of the overall energy absorption. Extremely low energy absorption occurs in the back plate of the tank, the ceramic layer, and the E36 plate. The overall plastic energy absorption of the protective structure decreases as the fragment weight increases.

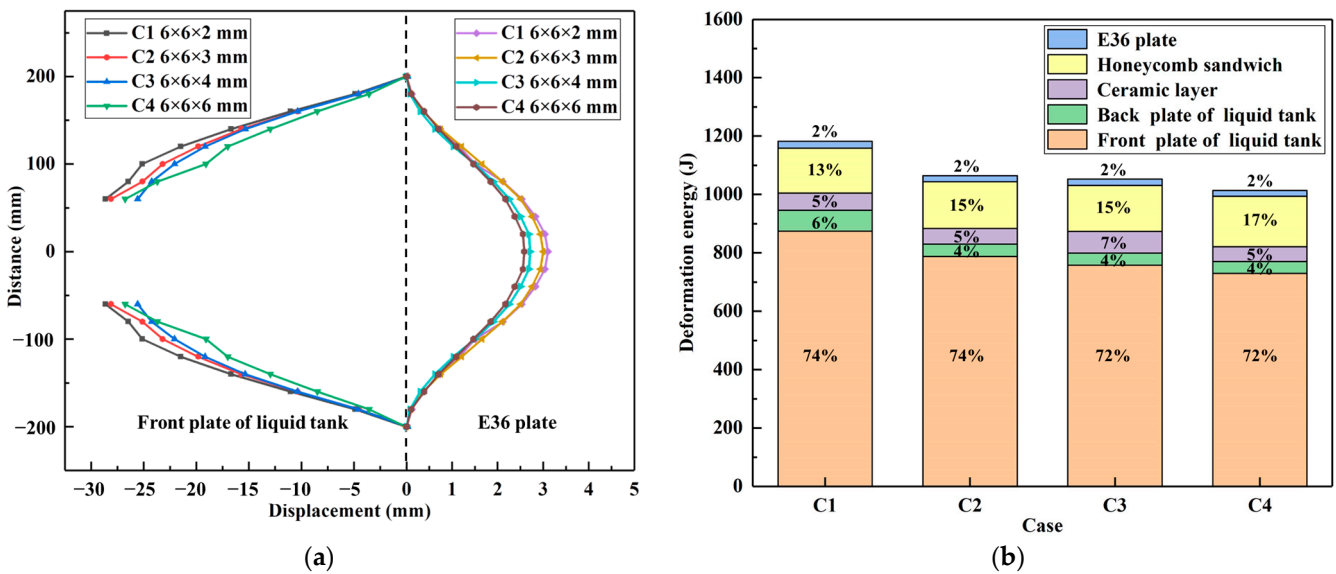


Figure 14. Structural response results under different fragment weights. (a) Final deformation of foremost and rearmost plates. (b) Energy of deformation absorption and its proportion of each layer structure.

3.3.2. Effect of Fragment Number

Figure 15a shows the specific distribution of fragments under the four conditions of C2, C5, C6 and C7; the numbers of fragments under the four conditions are 69, 49, 25 and 9. Figure 15b illustrates the velocity time history curves for various numbers of fragments. The observed variation in fragment velocity at the central position across the four conditions (ranging from 1300 m/s to 1400 m/s) is diminutive. This finding indicates that the energy dissipation of identically weighted and positioned fragments propelled by an equivalent charge mass is relatively consistent. There is a slight upward trend in the fragment velocity at the central position as the number of fragments increases. The augmented contact surface between the blast wave and the fragments is caused by the increased quantity of fragments. The velocities of edge fragments decrease significantly as the number of fragments increase under the four conditions. The velocity of edge fragments for C7 is only 75% of that for C2. As the distance from the edge to the center increases, the blast wave pressure decreases, the flip angle increases and the blast wave diffraction increases.

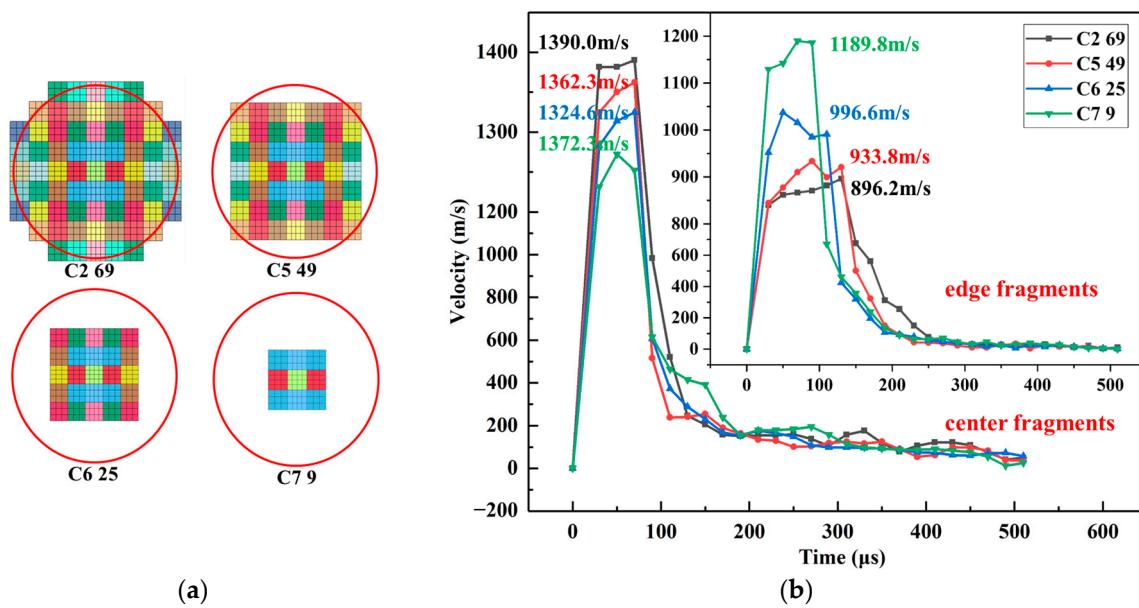


Figure 15. (a) Distribution of fragments with different numbers (Different colored squares are fragment groups). (b) Fragment velocity time history curve of different fragment numbers.

The ultimate response of the multilayer liquid-containing protective structure and the damage results of the front plate under different fragment numbers are illustrated in Figure 16. The results indicate that the damage mechanisms of each layer are essentially identical under the four conditions. The fragments pass through the liquid tank and penetrate the front plate. The water hammer effect induced by liquid cavitation induces a significant deflection on the front plate. The fragment fails to penetrate the back plate, resulting in the formation of impact marks. Under liquid extrusion, the ceramic layer and back plate deform backward, compressing the honeycomb structure and leading to local collapse failure and overall bending deformation. With the decrease in the number of fragments, the damage degree of the protective structure decreases gradually. The damage area of the front plate increases with the increase in the number of fragments. This phenomenon is primarily attributable to the fragment distribution position on the explosive. As the distance between the edge fragment and the explosive center increases, the final flight angles of the fragments increase.

Figure 17a illustrates the ultimate deformation of the E36 steel plate and the front plate subjected to varying numbers of fragments. The plastic deformation of the front plate undergoes significant variations as the number of fragments increases. The maximum plastic deformation at the central position increases from 14 mm under condition C7 to 28 mm under condition C2. The plastic deformation under condition C2 is essentially identical to that under condition C5. This phenomenon suggests that the overall deformation and energy absorption capacities of the front plate have reached their limits. The greatest deflection of the outermost E36 steel plate is less than 4 mm as the number of particles increases. The energy absorption ratio and deformation energy absorption for each layer of the protective structure are illustrated in Figure 17b. The energy absorption and energy absorption ratio of the front plate increase progressively with the increase in the number of fragments. These results indicate that the alteration in the number of fragments has the most significant influence on the front plate. As the number of fragments increases, there is a marginal decrease in the energy absorption ratio of the honeycomb layer. The expansion of the erosion failure area of the honeycomb structure results in a reduction in the overall deformation energy absorption ratio.

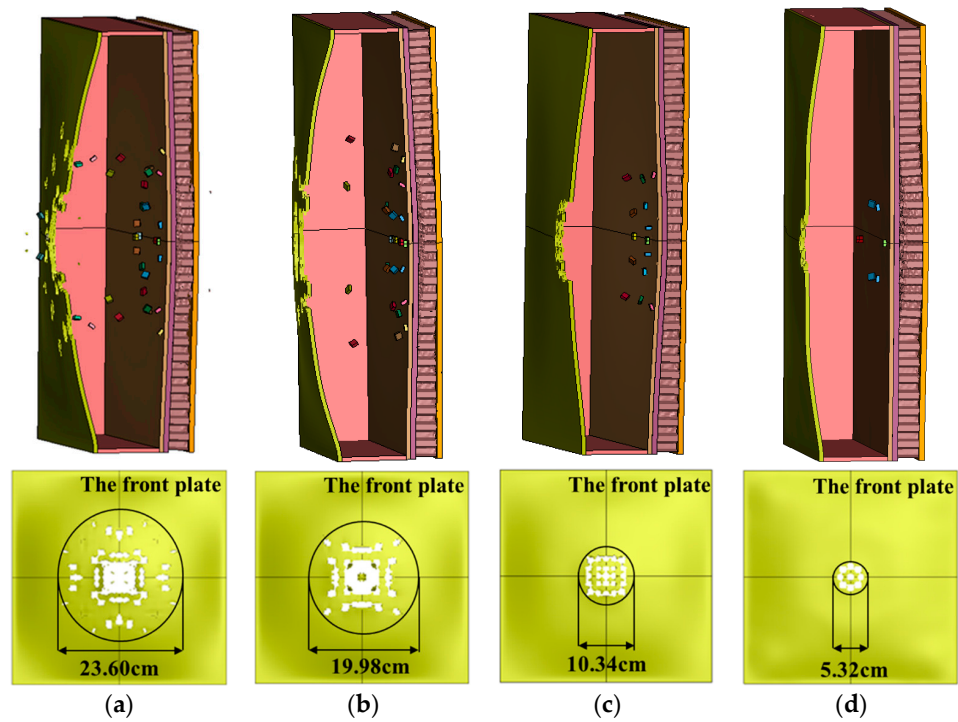


Figure 16. Ultimate response of multilayer liquid-containing protective structure and the damage results of the front plate under different fragment numbers. (a) C2—69; (b) C5—49; (c) C6—25; and (d) C7—9.

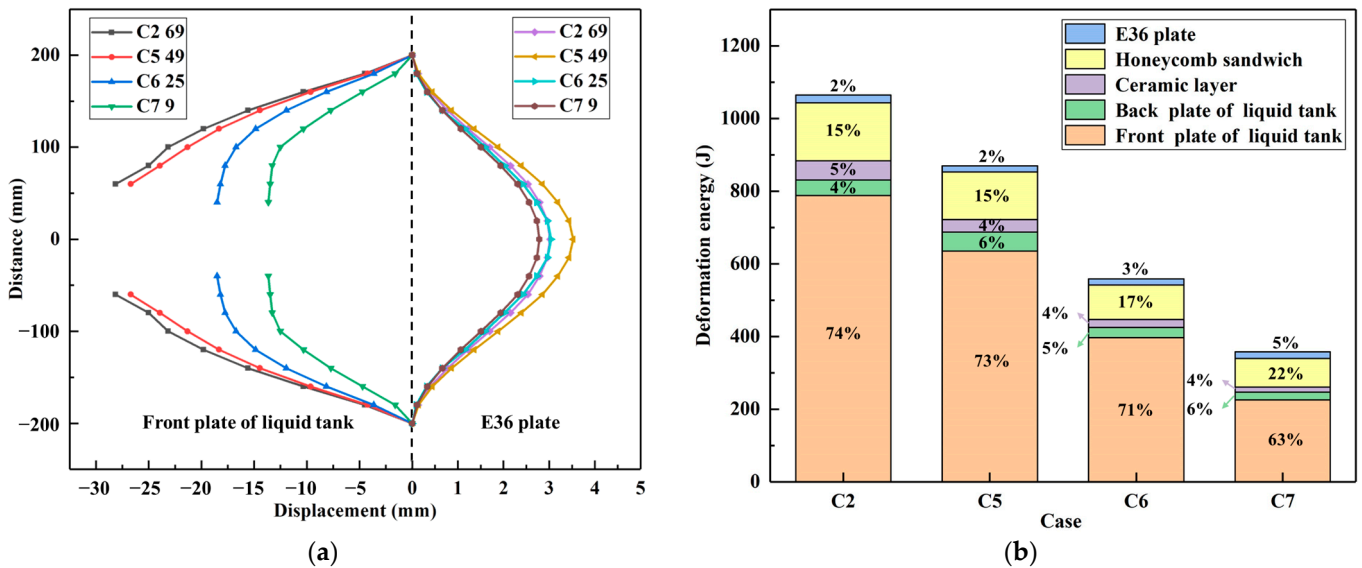


Figure 17. Structural response results under different fragment numbers. (a) Final deformation of foremost and rearmost plates. (b) Energy of deformation absorption and its proportion of each layer structure.

4. Conclusions

The purpose of this study is to evaluate the protection mechanisms of a multilayer liquid-containing protective structure under combined blast wave and fragment loading. The response process of the protective structure under combined loading is investigated. The degree of damage and the energy absorption of each layer are analyzed. Two crucial determinants that influence damage—charge mass and fragment form—are examined. The principal conclusions are as follows:

- (1) Under combined blast wave and fragment loading, the primary damage modes observed in each layer of the multilayer liquid-containing structure are as follows: A large central punching hole appears on the front plate of the liquid tank, followed by local fragment perforation and bulging bullet marks that extend sequentially from the center to the edge. Simultaneously, the entire structure undergoes substantial deflection deformation. The entire inward deflection deformation and a local fragment gunshot trace are visible on the back plate of the liquid tank. The ceramic layer forms cracks and local fractures. The honeycomb layer deforms as a whole with local collapse fails. The tank has the greatest absorptive capacity, followed by the honeycomb layer, and the front plate sustains the most severe damage. Due to fragments absorbing energy, the shape of the blast wave changes from spherical to ellipsoidal and to apple-shaped, and the water pressure is significantly greater than that of the air.
- (2) When all other variables remain constant, the velocity difference between the border fragment and the central fragment increases with increasing charge mass. As the charge mass increases, the explosion wave pressure in the air increases relatively slowly, while the blast wave pressure in the water varies significantly. The damage mode of the multilayer liquid-containing structure is primarily manifested as the expansion of the damage area on the front plate of the liquid tank and as the degree of compression collapse in the honeycomb layer as the charge mass increases. When the charge mass is small, fragments significantly impact the damage mode of the structure. When the equivalent charge mass is large, the damage effect of the blast wave becomes more pronounced.
- (3) When the charge mass remains constant, the degree of damage to the protective structure is minimally impacted by the fragment weight. The damage can be substantially reduced by decreasing the number of fragments. The overall plastic energy absorption and damage to the multilayer liquid-containing protective structure decrease as the fragment mass increases. However, the central region of the front plate sustains more severe damage. As the number of fragments increases, the absorption of plastic energy by the structure and the breakage of the front plate of the liquid tank increase significantly.

Author Contributions: Z.F.: investigation, validation, writing—original draft and formal analysis. X.L.: supervision, conceptualization, methodology, software, validation, formal analysis and writing—original draft. T.H.: writing—review and editing and validation. W.C.: writing—review and editing and supervision. All authors have read and agreed to the published version of the manuscript.

Funding: The research project was supported by the National Natural Science Foundation of China (grant numbers: 52201334; 51979213).

Institutional Review Board Statement: Not applicable.

Informed Consent Statement: Not applicable.

Data Availability Statement: The authors declare that the data presented in this study are available upon request.

Conflicts of Interest: The authors declare no conflict of interest.

References

1. Kurki, T. Contained Explosion inside a Naval Vessel—Evaluation of the Structure Response. Master's Thesis, Helsinki University of Technology, Helsinki, Finland, 2007.
2. Jiang, L.G.; Zhang, X.D. Destruction Analysis of Broadside Multi-Cabin Protective Structure of Warship under Explosion Loading. In *Proceedings of the Advanced Materials and Processes III, Pts 1 and 2*; Li, S., Li, W., Li, J., Eds.; University of Science and Technology Liaoning: Anshan, China; Metal Association Liaoning: Shenyang, China; Anshan Iron & Steel Group Corp.: Anshan, China; Saitama Institute of Technology: Saitama, Japan; Nanyang Technological University: Singapore; Chinese University of Hong Kong: Hong Kong, China; National Formosa University: Huwei, Taiwan, 2013; Volume 395–396, pp. 866–870.
3. Kong, X.; Wu, W.; Li, J.; Chen, P.; Liu, F. Experimental and Numerical Investigation on a Multi-Layer Protective Structure under the Synergistic Effect of Blast and Fragment Loadings. *Int. J. Impact Eng.* **2014**, *65*, 146–162. [[CrossRef](#)]

4. Li, M.; Hou, D.; Zhu, H.; Chen, X.; Li, C. Review on Ballistic Impact Resistance of Ship Armor Protection Structure. *Ship Build. China* **2018**, *59*, 237–250. (In Chinese)
5. Palomba, G.; Epasto, G.; Crupi, V. Lightweight Sandwich Structures for Marine Applications: A Review. *Mech. Adv. Mater. Struct.* **2021**, *29*, 4839–4864. [[CrossRef](#)]
6. Andreson, C.E., Jr. A Review of Computational Ceramic Armor Modeling. In *Advances in Ceramic Armor II: Ceramic Engineering and Science Proceedings*; The American Ceramic Society: Westerville, OH, USA, 2006; Volume 27, pp. 1–18.
7. Hazell, P.J.; Roberson, C.J.; Moutinho, M. The Design of Mosaic Armour: The Influence of Tile Size on Ballistic Performance. *Mater. Des.* **2008**, *29*, 1497–1503. [[CrossRef](#)]
8. Serjouei, A.; Gour, G.; Zhang, X.; Idapalapati, S.; Tan, G.E.B. On Improving Ballistic Limit of Bi-Layer Ceramic–Metal Armor. *Int. J. Impact Eng.* **2017**, *105*, 54–67. [[CrossRef](#)]
9. Zhu, F.; Zhao, L.; Lu, G.; Wang, Z. Deformation and Failure of Blast-Loaded Metallic Sandwich Panels—Experimental Investigations. *Int. J. Impact Eng.* **2008**, *35*, 937–951. [[CrossRef](#)]
10. Wu, X.; Yu, H.; Guo, L.; Zhang, L.; Sun, X.; Chai, Z. Experimental and Numerical Investigation of Static and Fatigue Behaviors of Composites Honeycomb Sandwich Structure. *Compos. Struct.* **2019**, *213*, 165–172. [[CrossRef](#)]
11. Wang, G.T.; Ning, Z.H.; Zhao, J.G.; Yang, L.M. Experimental Investigation on Deformation and Failure of Metallic Sandwich Panels under Blast Loading. *Mater. Res. Innov.* **2011**, *15*, S98–S101. [[CrossRef](#)]
12. Elanchezian, C.; Rammath, B.V.; Ramakrishnan, G.; Raghavendra, K.N.S.; Muralidharan, M.; Kishore, V. Review on Metal Matrix Composites for Marine Applications. *Mater. Today Proc.* **2018**, *5*, 1211–1218. [[CrossRef](#)]
13. Deng, Y.; Hu, X.; Yang, X.; Huang, Z.; Wang, Y.; Zhou, C. Dynamic Response of Nomex Honeycomb Sandwich Panels Subjected to Aluminum Foam Projectile Impact—An Experimental Study. *Polym. Compos.* **2023**, *44*, 1017–1037. [[CrossRef](#)]
14. Patel, M.; Patel, S. Influence of Honeycomb Core Height on the Blast Mitigation Performance of Sandwich Panel. *Mater. Today Proc.* **2023**, *74*, 611–620. [[CrossRef](#)]
15. Townsend, D.; Park, N.; Devall, P.M. Failure of Fluid Filled Structures Due To High Velocity Fragment Impact. *Int. J. Impact Eng.* **2003**, *29*, 723–733. [[CrossRef](#)]
16. Ji, Y.; Li, X.; Zhou, L.; Lan, X. Experimental and Numerical Study on the Cumulative Damage of Water-Filled Containers Impacted by Two Projectiles. *Thin-Walled Struct.* **2019**, *135*, 45–64. [[CrossRef](#)]
17. Ren, P.; Shi, L.; Ye, R.; Chai, D.; Zhao, W.; Wu, J.; Zhang, W.; Mu, Z. A Combined Experimental and Numerical Investigation on Projectiles Penetrating into Water-Filled Container. *Thin-Walled Struct.* **2019**, *143*, 106230. [[CrossRef](#)]
18. Xu, S.; Zhang, W.; Cai, Y.; Shen, W.; Wu, Y. Study on Anti-Penetration Performance of Kevlar Reinforced Honeycomb Liquid-Filled Cabin on Warship: Experimental Verification and Numerical Analysis. *Ocean Eng.* **2023**, *283*, 114959. [[CrossRef](#)]
19. Marchand, K.A.; Vargas, M.M.; Nixon, J.D. *The Synergistic Effects of Combined Blast and Fragment Loadings*; Southwest Research Institute: San Antonio, TX, USA, 1992.
20. Nyström, U.; Gylltoft, K. Numerical Studies of the Combined Effects of Blast and Fragment Loading. *Int. J. Impact Eng.* **2009**, *36*, 995–1005. [[CrossRef](#)]
21. Zhang, C.; Cheng, Y.; Zhang, P.; Duan, X.; Liu, J.; Li, Y. Numerical Investigation of the Response of I-Core Sandwich Panels Subjected to Combined Blast and Fragment Loading. *Eng. Struct.* **2017**, *151*, 459–471. [[CrossRef](#)]
22. Cai, S.; Liu, J.; Zhang, P.; Li, C.; Cheng, Y.; Chen, C. Experimental Study on Failure Mechanisms of Sandwich Panels with Multi-Layered Aluminum Foam/UHMWPE Laminate Core under Combined Blast and Fragments Loading. *Thin-Walled Struct.* **2021**, *159*, 107227. [[CrossRef](#)]
23. Li, L.; Jia, F.; Liu, L.; Yu, R.; Zhang, Q.; Li, L. Response of Aluminium Honeycomb Sandwich Panels under Combined Shock and Impact Loading: Experimental and Numerical Investigations. *Thin-Walled Struct.* **2023**, *193*, 111256. [[CrossRef](#)]
24. Jin, J.; Hou, H.; Chen, P.; Zhu, X.; Li, D. Experimental Study on the Combined Damage of Liquid Cabin Structure Subjected to Charge Explosion with Preset Fragments. *Int. J. Impact Eng.* **2019**, *130*, 19–26. [[CrossRef](#)]
25. Huang, T.; Chen, W.; Peng, S.; Shi, R.; Chai, W.; Li, X. Testing Investigation on Load and Damage Characteristic of Typical Cabins under Warhead Internal Blast. *Chin. J. Ship Res.* **2023**, *19*, 1–12. (In Chinese) [[CrossRef](#)]
26. Gupta, Y.M.; Ding, J.L. Impact Load Spreading in Layered Materials and Structures: Concept and Quantitative Measure. *Int. J. Impact Eng.* **2002**, *27*, 277–291. [[CrossRef](#)]
27. Tang, H.M.; Tang, R.T.; Wen, H.M. Predicting the Perforation of Ceramic-Faced Light Armors Subjected to Projectile Impact. *Int. J. Impact Eng.* **2017**, *102*, 55–61. [[CrossRef](#)]
28. Tao, Y.; Duan, S.; Wen, W.; Pei, Y.; Fang, D. Enhanced Out-of-Plane Crushing Strength and Energy Absorption of In-Plane Graded Honeycombs. *Compos. Part B Eng.* **2017**, *118*, 33–40. [[CrossRef](#)]
29. Zhang, Y.; Mao, W.; Yang, L.-W.; Li, K. Dynamic Mechanical Behavior and Constitutive Relation of Shipbuilding E36 Steel. *Chuan Bo Li Xue/J. Ship Mech.* **2022**, *26*, 912–918. (In Chinese)
30. International Symposium on Ballistics; National Defense Industrial Association; International Ballistics Committee. Characterization of Al 6061-T6 Using Split Hopkinson Bar Tests and Numerical Simulations. In *Proceedings of the 22nd International Symposium on Ballistics*, Vancouver, BC, Canada, 14–18 November 2005; Volume 2.
31. Feng-Kui, C.; Chao, G.; Yu-Xi, L.I. Flow Stress Characteristics and Dynamic Constitutive Model for 40Cr Steel. *J. Henan Univ. Sci. Technol. Nat. Sci.* **2012**, *5*, 1–5. (In Chinese)

32. Cronin, D.S.; Bui, K.; Kaufmann, C.; Mcintosh, G.; Berstad, T. Implementation and Validation of the Johnson-Holmquist Ceramic Material Model in LS-DYNA. In Proceedings of the 4th European LS-DYNA User's Conference, Ulm, Germany, 22–23 May 2003.
33. Luccioni, B.M.; Ambrosini, R.D. Evaluating the Effect of Underground Explosions on Structures. *Mecánica Comput.* **2008**, *25*, 1999–2019.
34. Cheng, D.S.; Hung, C.W.; Pi, S.J. Numerical Simulation of Near-Field Explosion. *Tamkang J. Sci. Eng.* **2013**, *16*, 61–67.
35. Kim, M.-S.; Kim, C.-Y.; Song, M.-K.; Lee, S.S. Assessment of the Blasting Efficiency of a Long and Large-Diameter Uncharged Hole Boring Method in Tunnel Blasting Using 3D Numerical Analysis. *Sustainability* **2022**, *14*, 13347. [[CrossRef](#)]
36. Li, J.; Huang, C.; Ma, T.; Huang, X.; Li, W.; Liu, M. Numerical Investigation of Composite Laminate Subjected to Combined Loadings with Blast and Fragments. *Compos. Struct.* **2019**, *214*, 335–347. [[CrossRef](#)]
37. LI, S.; LI, X.; HU, X. Research into Energy Absorption of Liquid Cabin Subjected to Close-Range Explosion. *Chin. J. Ship Res.* **2017**, *12*, 101–106. (In Chinese) [[CrossRef](#)]
38. Zhong, Q.; Hou, H.L.; Li, D. Experimental Study on Anti-Penetration Mechanism of Ceramic/Fluid Cabin Composite Structure. *Chuan Bo Li Xue/J. Ship Mech.* **2017**, *21*, 1282–1290.

Disclaimer/Publisher's Note: The statements, opinions and data contained in all publications are solely those of the individual author(s) and contributor(s) and not of MDPI and/or the editor(s). MDPI and/or the editor(s) disclaim responsibility for any injury to people or property resulting from any ideas, methods, instructions or products referred to in the content.